Global ocean heat transport dominated by heat export from the tropical Pacific

Gaël Forget [ID][1]* and David Ferreira [ID][2]

Heat redistribution is one of the main mechanisms by which oceans regulate Earth's climate. Analyses of ocean heat transport tend to emphasize global-scale seawater pathways and concepts such as the great ocean conveyor belt. However, it is the divergence or convergence of heat transport within an oceanic region, rather than the origin or destination of seawater transiting through that region, that is most immediately relevant to Earth's heat budget. Here we use a recent gridded estimate of ocean heat transport to reveal the net effect on Earth's heat budget, the 'effective' ocean heat transport, by removing internal ocean heat loops that have obscured the interpretation of measurements. The result demonstrates the overwhelming predominance of the tropical Pacific, which exports four times as much heat as is imported in the Atlantic and Arctic. It also highlights the unique ability of the Atlantic and Indian oceans to transport heat across the Equator—Northward and Southward, respectively. However, effective inter-ocean heat transports are smaller than expected, suggesting that global-scale seawater pathways play only a minor role in Earth's heat budget.

The ocean plays an important role in redistributing heat within the evolving climate system[1]. Perhaps most importantly, it transports heat from the Equator, where oceans take up heat in excess, towards higher latitudes where heat gets released to the atmosphere. This is clearly seen in observational estimates of meridional ocean heat transport (OHT) integrated all the way around the Earth, which is directed poleward in both hemispheres[2–4]. However, interpretation of measurements can be more difficult when looking at individual ocean basins and sections as seawater can loop around land masses in complicated ways without immediately affecting the atmosphere. This complexity has led to high uncertainties in regional OHT analyses[5]. Here we provide a framework to help reconcile previous estimates.

The two following examples illustrate how some regional OHT contributions can play an important role in Earth's energy budget while others may just reflect mass fluxes within the ocean. First, consider a scenario where OHT converges into an ocean basin to balance out heat release to the atmosphere. Such OHT plays an immediate role in Earth's energy budget[2,6,7]. Second, imagine seawater looping around in the ocean interior, for example, eastward around Antarctica, and with unchanged temperatures. This mass flux carries internal energy (for example, temperature) that contributes to OHT but has no impact on Earth's energy budget until heat is exchanged with the atmosphere and maybe after looping around Antarctica many times[8]. A detailed understanding of seawater pathways is often useful to analyse the climate system's behaviour but a key point here is that the atmosphere feels the effect of OHT only through air–sea fluxes.

Any ocean section can be affected by mass fluxes in ways that are not easy to predict given the complex, present-day arrangement of land masses. Freshwater may also temporarily leave the ocean via evaporation to re-enter it elsewhere via precipitation, and closing such ocean–atmosphere loops[9] can, in and of itself, introduce non-zero mass fluxes throughout the ocean. As a result, OHT through any individual section is a priori sensitive to the observer's choice of an energy reference level (ERL; for example, temperature at which

energy is defined as zero). Let us assume, for example, that water parcels looping around Antarctica have a temperature of 2 °C. If the observer chooses an ERL at 0 °C, then this internal OHT is viewed as positive (eastward), but the same OHT is instead viewed as negative (westward) with an ERL at 4 °C, or as zero with an ERL at 2 °C. Hence, individual OHT values can be arbitrary and just reflect an observer's ERL choice—a choice that, of course, does not affect the climate system itself.

Progress can be made, however, through the decomposition of plain OHT (OHT_0) into an 'effective' OHT that balances heat exchanges with the atmosphere (OHT_∇) and a second term representing internal ocean heat loops that do not immediately affect Earth's energy budget ($OHT_{R,0}$). In mathematical terms, we carry out a Helmholtz decomposition of OHT_0 into divergent (OHT_∇) and rotational ($OHT_{R,0}$) components. This decomposition is applied to a state-of-the-art global, gridded data product (see Methods). An important point is that OHT_∇, unlike OHT_0 or $OHT_{R,0}$, is insensitive to mass fluxes and the chosen ERL (0 °C, here). OHT_∇ represents the net effect of OHT as experienced by the atmosphere via air–sea fluxes rather than seawater pathways.

Transport maps

Values of OHT_0 and OHT_∇ are coarsely charted in Fig. 1 (see Supplementary Tables for further detail). The OHT_0 values generally fit well within the range of previously published 'direct' estimates from ocean sections[5,10–13], whereas the OHT_∇ values correspond to 'indirect' estimates derived from air–sea flux maps[4–7]. Both OHT_0 and OHT_∇ yield the exact same divergence field (contours in Fig. 1). For example, 1.46 PW diverges from the tropical Pacific box bounded by 30° S and 30° N while 0.11 PW converges into the Atlantic sector (90° S to ~60° N) for both the blue and the red charts in Fig. 1. They are also identical when globally integrated (black curve in Fig. 2). Nevertheless, OHT_0 and OHT_∇ provide fundamentally different perspectives on regional OHT contributions, due to the prominence of ocean heat loops in OHT_0, as evidenced by Fig. 1.

[1]Department of Earth, Atmospheric and Planetary Sciences, Massachusetts Institute of Technology, Cambridge, MA, USA. [2]Department of Meteorology, University of Reading, Reading, UK. *e-mail: gforget@mit.edu
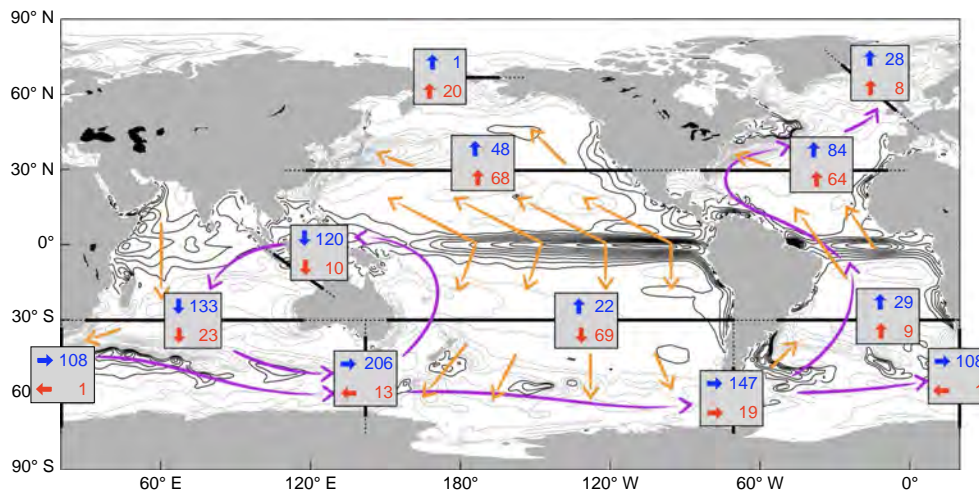
Fig. 1 | OHT as estimated through sections that separate ocean basins and delimit the tropics for the 1992–2011 time average. Values (in 0.01 PW = 10^{13} Watts) of plain OHT (rotational + divergent components; OHT_0) and effective OHT (divergent component alone; OHT_∇) are charted in blue and in red, respectively. The thin lines with arrowheads are a schematic of internal ocean heat loops (purple) and effective OHT patterns (orange). The black contours (respectively, grey contours) represent the rate of OHT divergence (respectively, convergence), which corresponds to heat uptake from (respectively, heat release to) the atmosphere. These rates are contoured every 15 W m⁻² starting from ±5 W m⁻².
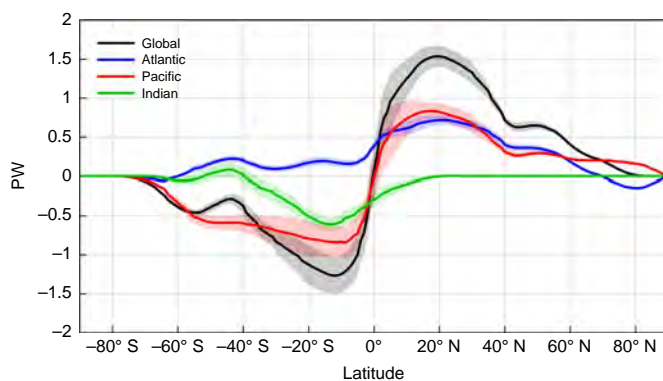

Fig. 2 | Meridional effective OHT. The global ocean case is depicted in black. Meridional effective OHT for the Atlantic (blue), Pacific (red) and Indian (green) sectors is also shown. The thick lines denote the 1992–2011 time average and the shaded ranges reflect ±1 standard deviation among annual means.

Owing to the presence of the Atlantic Meridional Overturning Circulation (AMOC), which brings relatively warm water into the Northern Hemisphere and returns colder water back into the Southern Hemisphere, Atlantic OHT is northward across the Equator and in both hemispheres[13–15]. This is true for both OHT_0 and OHT_∇, as seen in Fig. 1 and Supplementary Fig. 1. In the Pacific, large amounts of heat enter the ocean through the sea surface in the tropics (black contours in Fig. 1). Based on OHT_0, most of this heat uptake (1.20 PW) appears to be transported to the Indian Ocean via the Indonesian through flow (ITF).

The Southern Ocean also stands out for its large eastward OHT_0, with values ranging between about 1 and 2 PW seen around Antarctica. However, OHT_0 values are highly sensitive to ERL choices, so much so that setting ERL to 3.5 °C, the approximate global mean ocean temperature, instead of 0 °C, suffices to reverse the direction of OHT_0 throughout the Southern Ocean. This is not the case for OHT_∇, which is much less affected by non-zero mass fluxes as demonstrated in the Supplementary Information (see Methods).

Eliminating ocean heat loops ($OHT_{R,0}$) reduces inter-ocean exchanges to second-order terms (OHT_∇; red chart in Fig. 1). The Pacific thus merely provides ~0.2 PW to each of the Atlantic, Arctic and Indian. OHT_∇ clearly reveals that OHT divergence from the tropical Pacific (1.8 PW) is much larger than OHT convergence in the Atlantic and pan-Arctic (0.40 PW). The ratio between these two terms is 4.5 in the gridded ocean estimate (Fig. 1) and 4.4 in the ensemble average of inferred estimates (see Methods). Hence, a new paradigm emerges from OHT_∇ that emphasizes heat redistribution within ocean basins rather than through global-scale circulations[1,16].

It is striking that the direction of OHT_∇ in the South Pacific is reversed as compared with OHT_0 (poleward instead of equatorward) and that poleward OHT_∇ is much smaller than OHT_0 would suggest in the Indian (0.23 versus 1.33 PW at 30° S; a factor ~6 reduction). These differences are linked to a known anticlockwise loop of ocean circulation around Australia[13,16,17]. Omitting this heat loop suggests that the net effect of the ITF as part of Earth's energy budget is as small as 0.10 PW. In the Southern Ocean, at all longitudes, OHT_∇ is also much smaller than OHT_0 due to the omission of a heat loop that goes around Antarctica.

Westward OHT_∇ between Australia and Antarctica indicates that heat loss in the Indian balances out heat gained in the Pacific—not the other way around as might have been inferred from eastward OHT_0 values[18,19]. Pacific to Atlantic OHT_∇ accounts for about half of the heat convergence into the South Atlantic, while the rest is provided by local heat uptake from the atmosphere. There is virtually no OHT_∇ between the Indian and Atlantic (0.01 PW), which indicates a near-exact cancellation among westward and eastward contributions across the Africa–Antarctica section[16].

Meridional transports

The respective roles played by the Atlantic, Pacific and Indian in transporting heat poleward also need to be revisited (Fig. 2). Estimates of OHT_0 notably suggest that only the Indian Ocean transports heat poleward in the Southern Hemisphere (for example, see the blue chart in Fig. 1). On the contrary, poleward OHT_∇ in the South Pacific (0.69 PW at 30° S) is three times that in the Indian (0.23 PW at 30° S; see Figs. 1 and 2). Poleward OHT_∇ in the South Pacific is robust across all inferred estimates shown in the Supplementary Information (Supplementary Fig. 7), with an
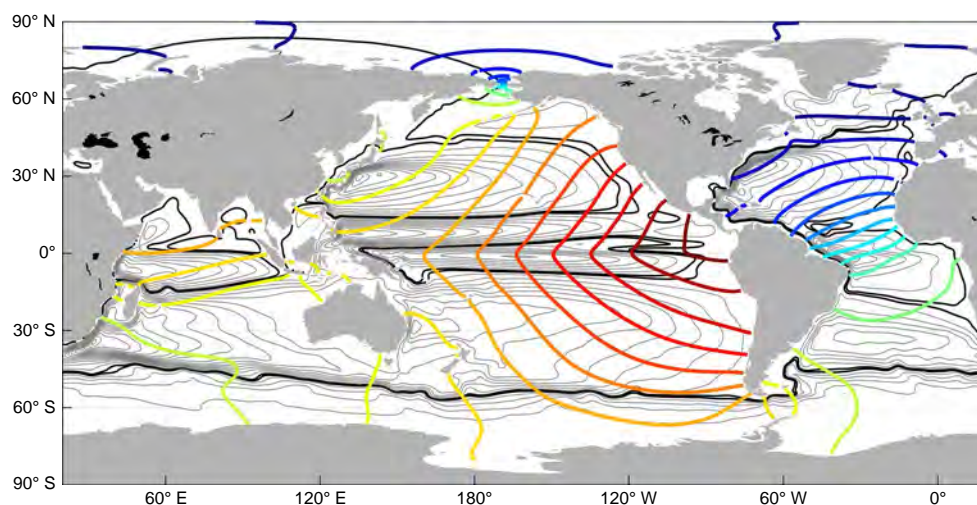
Fig. 3 | Scalar potential and vector potential as derived from the global vector field of OHT_0 for the 1992–2011 time average. The divergent (OHT_∇) and rotational ($OHT_{R,0}$) components of OHT_0 are associated with, respectively, the scalar potential (coloured contours; in 0.2 PW intervals) and the vector potential (black and grey contours; in 0.05 and then 0.2 PW intervals) (see Methods). Each contour of the vector potential can be thought of as a heat loop confined within the ocean. In contrast, OHT_∇ is oriented perpendicularly across contours of the scalar potential. Positive OHT_∇ goes from red to blue contours.

ensemble average of 0.55 PW at 30° S, and consistent with previous OHT analyses[7,13]. Furthermore, symmetry between the two hemispheres becomes evident in the Pacific through OHT_∇, with poleward transport of ~0.7 PW at 30° N and 30° S, and negligible cross-equatorial transport (Supplementary Table 3).

The largest inter-hemispheric OHT_∇ is found in the Atlantic where 0.39 PW crosses the Equator in the gridded ocean estimate (0.60 PW in the inferred estimates ensemble average). This 0.39 PW approximately balances out: 0.27 PW atmospheric heat uptake in the southern Atlantic sector plus 0.19 PW provided by the Pacific; and 0.34 PW heat loss to the atmosphere in the North Atlantic plus 0.09 PW exiting towards the Arctic. Subtracting 0.39 PW from OHT_∇ throughout the Atlantic in turn yields an estimate of 0.33 PW (respectively, 0.30 PW) for the northern (respectively, southern) subtropical wind-driven cell.

These results are consistent with previous findings that the inter-hemispheric, AMOC-related, OHT represents only ~50% of the peak OHT in the Atlantic[13,15]. Interestingly, 0.30–0.33 PW per subtropical wind-driven cell for the Atlantic is ~50% of the corresponding Pacific value (~0.7 PW). Such proportionality is hypothesized to reflect that the Pacific is about twice as wide as the Atlantic along the Equator where ocean heat uptake is concentrated. Hence, the gyre systems of the Pacific and Atlantic appear to redistribute tropical heat uptake with similar efficiency.

Most of the heat converging into the pan-Arctic (0.20 PW out of 0.29 PW) is attributed to the Pacific directly as OHT_∇ at Bering Strait. The other 0.09 PW is assigned to Atlantic passages towards the Arctic, but it is also ultimately attributed to the Pacific as part of the 0.19 PW that it provides to the South Atlantic. It is noteworthy that the magnitude of these two contributions appears quite robust across OHT_∇ estimates (0.26 and 0.14 PW, respectively, in the inferred estimates ensemble average; see Supplementary Table 9). However, nothing in our analysis excludes that heat taken up in the Pacific may have to transit via the Atlantic to eventually reach the Arctic.

Ocean heat loops

The rotational OHT component estimate ($OHT_{R,0} = OHT_0 - OHT_\nabla$; grey contours in Fig. 3) provides a simplified, two-dimensional depiction of seawater pathways that are not informed by OHT_∇.

This global mapping of ocean heat loops highlights familiar features of the wind-driven ocean circulation that connect and can even shape regions of air–sea heat uptake and loss[17,20–22]. $OHT_{R,0}$, for instance, clearly reflects subtropical gyres, which are associated with shallow overturning circulations that set up the global hemispheric pattern of poleward OHT[15], and can often help interpret OHT_∇. The westward orientation of OHT_∇ at mid-latitudes (OHT_∇ goes from red to blue contours in Fig. 3) is notably thought to reflect that subtropical gyres release heat, which they take up in the tropics, to the atmosphere primarily via western boundary currents and associated mode water formation sites[23].

$OHT_{R,0}$ is divergence-free and equal to zero when integrated all the way around the Earth, but often large on a regional scale. For example, heat loops around Australia and Antarctica are found to contribute, respectively, $OHT_{R,0} \approx 1.1$ PW in the ITF and $OHT_{R,0} \approx 1.3$ PW at Drake Passage. These estimates mostly reflect an arbitrary ERL choice but their importance should not be overlooked—they open the possibility for more meaningful comparison among OHT estimates. For example, adding $OHT_{R,0}$ to OHT_∇ estimates inferred from air–sea heat flux maps (for example, Supplementary Fig. 7) will allow for direct comparison with ship-based OHT_0 estimates in future studies.

A remaining challenge is the need to quantify $OHT_{R,0}$ uncertainties associated with limited ocean data coverage and imperfect estimation methods. We do not currently know how uncertain the Fig. 3 estimate of $OHT_{R,0}$ is, but we suggest that applying our decomposition methodology to an ensemble of gridded OHT_0 products[24] could help resolve this issue. It may also be worth stressing that closed circulation concepts, such as the great conveyor belt, stream functions or indeed $OHT_{R,0}$, should not be taken literally but rather viewed as simplifications of a complex system that permit scientific insight. In reality seawater does not experience perfectly closed pathways because of temporal variability, chaotic turbulence and many other complicating factors.

Complementary analysis methods remain needed as our two-dimensional framework is bound to have limitations and should not be mistaken for a comprehensive description of the full three-dimensional, time-variable structure of ocean transports. For example, the shift between OHT_∇ and OHT_0 in the Northern Hemisphere (Supplementary Fig. 1) corresponds to a heat loop of ~0.2 PW that

goes northward in the Atlantic, crosses the Arctic and comes back southward in the Indo-Pacific. However, this interpretation is not entirely satisfying because the direct mass flux through Bering Strait is only ~10^6 m^3 s^{-1}, and this leads us to conclude that three-dimensional pathways will have to be examined to understand precisely how heat transits between the Pacific and the Arctic.

In summary, this study bridges a gap between two contrasting depictions of OHT that emerge either from an atmospheric perspective focused on air–sea fluxes[4] or from an oceanic perspective focused on observed sections[3]. By deriving both of them from the same gridded data product we show that apparent conflicts among earlier estimates in part reflect comparison of different entities (see Fig. 1 and Supplementary Tables). Importantly, a new perspective on the net effect of OHT within the coupled climate system has emerged from this decomposition.

Net ocean heat redistribution takes place primarily within oceanic basins and to a lesser extent through exchanges between basins. The Pacific predominates in terms of Equator-to-pole heat redistribution in both hemispheres, as it is wider in the tropics where heat is received from above. The Atlantic and Indian, however, play a unique role in transporting heat across the Equator. Their lack of symmetry between hemispheres is associated with the presence of the AMOC in the Atlantic and of land to the north of the Indian. While concepts such as the great conveyor belt are often highlighted in the OHT literature, our analysis instead emphasizes that heat redistribution within the Pacific is the largest term. This result stresses that sustained observation of the global ocean as a whole, not just at a few locations and gates separating ocean basins, is crucial to monitor and understand OHT.

Online content

Any methods, additional references, Nature Research reporting summaries, source data, statements of data availability and associated accession codes are available at https://doi.org/10.1038/s41561-019-0333-7.

References

1. Stocker, T. F. in *Ocean Circulation and Climate* (eds Siedler, G. et al.) Ch. 1 (International Geophysics Vol. 103, Academic Press, 2013).
2. Trenberth, K. E. & Solomon, A. The global heat balance: heat transports in the atmosphere and ocean. *Clim. Dyn.* **10**, 107–134 (1994).
3. Ganachaud, A. & Wunsch, C. Improved estimates of global ocean circulation, heat transport and mixing from hydrographic data. *Nature* **408**, 453–457 (2000).
4. Trenberth, K. E. & Caron, J. M. Estimates of meridional atmosphere and ocean heat transports. *J. Clim.* **14**, 3433–3443 (2001).
5. Macdonald, A. M. & Baringer, M. O. in *Ocean Circulation and Climate* (eds Gerold Siedler, J. G. et al.) Vol. 103 Ch. 29 (Academic Press, 2013).
6. Fasullo, J. T. & Trenberth, K. E. The annual cycle of the energy budget. part II: meridional structures and poleward transports. *J. Clim.* **21**, 2313–2325 (2008).
7. Trenberth, K. E. & Fasullo, J. T. Atlantic meridional heat transports computed from balancing Earth's energy locally. *Geophys. Res. Lett.* **44**, 1919–1927 (2017).
8. Tamsitt, V. et al. Spiraling pathways of global deep waters to the surface of the Southern Ocean. *Nat. Commun.* **8**, 172 (2017).
9. Döös, K. et al. The coupled ocean–atmosphere hydrothermohaline circulation. *J. Clim.* **30**, 631–647 (2017).
10. Ganachaud, A. & Wunsch, C. Large-scale ocean heat and freshwater transports during the world ocean circulation experiment. *J. Clim.* **16**, 696–705 (2003).
11. Johns, W. E. et al. Continuous, array-based estimates of Atlantic Ocean heat transport at 26.5°N. *J. Clim.* **24**, 2429–2449 (2011).
12. Lumpkin, R. & Speer, K. Global ocean meridional overturning. *J. Phys. Oceanogr.* **37**, 2550–2562 (2007).
13. Talley, L. D. Shallow, intermediate, and deep overturning components of the global heat budget. *J. Phys. Oceanogr.* **33**, 530–560 (2003).
14. Boccaletti, G., Ferrari, R., Adcroft, A., Ferreira, D. & Marshall, J. The vertical structure of ocean heat transport. *Geophys. Res. Lett.* **32**, L10603 (2005).
15. Ferrari, R. & Ferreira, D. What processes drive the ocean heat transport? *Ocean Model.* **38**, 171–186 (2011).
16. Speich, S. et al. Tasman leakage: a new route in the global ocean conveyor belt. *Geophys. Res. Lett.* **29**, 55-1–55-4 (2002).
17. Hirst, A. C. & Godfrey, J. The role of Indonesian throughflow in a global ocean GCM. *J. Phys. Oceanogr.* **23**, 1057–1086 (1993).
18. Sun, C. & Watts, D. R. Heat flux carried by the Antarctic Circumpolar Current mean flow. *J. Geophys. Res. C* **107**, 2-1–2-13 (2002).
19. Tamsitt, V., Talley, L. D., Mazloff, M. R. & Cerovečki, I. Zonal variations in the Southern Ocean heat budget. *J. Clim.* **29**, 6563–6579 (2016).
20. Godfrey, J. S. A sverdrup model of the depth-integrated flow for the world ocean allowing for island circulations. *Geophys. Astrophys. Fluid Dyn.* **45**, 89–112 (1989).
21. Song, Q., Vecchi, G. A. & Rosati, A. J. The role of the Indonesian throughflow in the Indo-Pacific climate variability in the GFDL coupled climate model. *J. Clim.* **20**, 2434–2451 (2007).
22. Corell, H., Nilsson, J., Döös, K. & Broström, G. Wind sensitivity of the inter-ocean heat exchange. *Tellus A* **61**, 635–653 (2009).
23. Speer, K. & Forget, G. in *Ocean Circulation and Climate* (eds Siedler, G. et al.) Vol. 103 Ch. 9 (Academic Press, 2013).
24. Balmaseda, M. et al. The Ocean Reanalyses Intercomparison Project (ORA-IP). *J. Oper. Oceanogr.* **8**, s80–s97 (2015).

Acknowledgements

Author contributions

G.F. performed the analyses and wrote the manuscript. Both authors contributed to the design of the study and interpretation of the results.

Competing interests

The authors declare no competing interests.

Additional information

Supplementary information is available for this paper at https://doi.org/10.1038/s41561-019-0333-7.

Reprints and permissions information is available at www.nature.com/reprints.

Correspondence and requests for materials should be addressed to G.F.

Publisher's note: Springer Nature remains neutral with regard to jurisdictional claims in published maps and institutional affiliations.

Methods

The need to adequately account for non-zero mass fluxes when analysing OHT through sections has long been recognized in the oceanographic literature, where various approaches have been proposed[25,26]. One method is to adjust the net mass flux through individual sections to near zero[10,11]. Another consists of pairing various sections with, for example, Bering Strait or the ITF aiming to cancel out non-zero mass flux contributions[5,13]. Alternatively, in cases such as the Antarctic Circumpolar Current where adjusting to zero mass flux is not sensible and there are not obvious pairing sections, one may opt to introduce a distinctive temperature transport scale sometimes denoted as 'PWT'[5,13]. In the ITF literature, the concept of a transport-weighted temperature is also sometimes invoked[27]. These heterogeneous treatments of OHT, however, can render comparison among estimates difficult and contribute to large uncertainties and unexplained differences between estimates[5,7]. Here we provide an alternative framework that can help reconcile OHT estimates.

The Decomposition method section introduces the method used to derive effective OHT (OHT_∇) and the ocean heat loops component ($OHT_{R,0}$) through a decomposition of plain OHT (OHT_0). The Gridded data product section in turn introduces the global, gridded OHT_0 estimate used in this study. Next, the ERL and Heat budget sections demonstrate two fundamental properties of OHT_∇. Firstly, unlike OHT_0 and $OHT_{R,0}$, it is insensitive to the ERL choice (here, 0 °C). Secondly, its divergence balances out regional air–sea heat fluxes to a very good approximation for climatological time averages. The Estimate uncertainty section then takes advantage of this property and evaluates OHT_∇ uncertainties on the basis of an ensemble of mapped air–sea heat flux estimates. Finally, the Improved method section shows that the new method avoids artefacts seen in previous studies that inferred OHT from air–sea heat fluxes.

Decomposition method. As is classically done in Helmholtz decomposition, we separate a vector field $\mathbf{F}$, defined over the global ocean, into a divergent component, $\mathbf{F}_{\mathrm{div}}$, and a rotational component, $\mathbf{F}_{\mathrm{rot}}$, that satisfy equations (1) and (2).

$$\mathbf{F} = \mathbf{F}_{\mathrm{div}} + \mathbf{F}_{\mathrm{rot}} \tag{1}$$

$$\nabla \times \mathbf{F}_{\mathrm{div}} = 0 \text{ and } \nabla \cdot \mathbf{F}_{\mathrm{rot}} = 0 \tag{2}$$

The divergent and rotational components are associated with, respectively, a scalar potential, $\mathcal{P}$, and a streamfunction, $\mathcal{S}$, as expressed in equations (3) and (4).

$$\mathbf{F}_{\mathrm{div}} = \nabla \mathcal{P} \tag{3}$$

$$\mathbf{F}_{\mathrm{rot}} = \nabla \times \mathcal{S} \tag{4}$$

In practice, $\mathcal{P}$ is computed by solving equation (5) over the global ocean.

$$\nabla^2 \mathcal{P} = \nabla \cdot \mathbf{F} \tag{5}$$

This Poisson equation is obtained by taking the divergence of equation (1) and then substituting equations (2) and (3). The divergent component, $\mathbf{F}_{\mathrm{div}}$, then readily derives from $\mathcal{P}$ via equation (3), the rotational component is computed as the remainder of equation (1), $\mathbf{F}_{\mathrm{rot}} = \mathbf{F} - \mathbf{F}_{\mathrm{div}}$, and integration of the transverse component of $\mathbf{F}_{\mathrm{rot}}$ following grid line paths gives $\mathcal{S}$ in equation (4).

The Poisson equation is formulated such that $\mathbf{F}_{\mathrm{div}}$ obeys a zero normal flow boundary condition at the coastline over the global ocean. This choice makes the most immediate physical and practical sense[28]. Since the same boundary condition is satisfied for $\mathbf{F}$, it also holds true for $\mathbf{F}_{\mathrm{rot}} = \mathbf{F} - \mathbf{F}_{\mathrm{div}}$, which means that $\mathbf{F}$, $\mathbf{F}_{\mathrm{div}}$ and $\mathbf{F}_{\mathrm{rot}}$ are all tangential to the coastline. The decomposition of $\mathbf{F}$ as $\mathbf{F}_{\mathrm{div}} + \mathbf{F}_{\mathrm{rot}}$ thus yields a simple extension of the familiar notion of meridional transports bounded by coastlines (for example, Supplementary Fig. 1).

Similar Helmholtz decomposition techniques have been used in the atmospheric and oceanic literature to decompose various fluxes[2,22,28,29]. This study presents a novel application of this approach to an observational OHT estimate (see Gridded data product). The Poisson equation approach is also used in the Heat budget and Estimate uncertainty sections, below, to interpret heat budgets and air–sea fluxes in terms of OHT. All required functionalities, including the Poisson equation solver, are provided by the gcmfaces toolbox[30,31].

Gridded data product. Our analysis is based on the ECCO version 4 release 2 gridded data product[30,32–35]. This ocean state estimate agrees, within uncertainty ranges, with the bulk of available ocean observations as well as with atmospheric reanalysis data over 1992–2011. It includes a full set of optimized transport estimates across the sea surface and in the ocean interior along with recent estimate of geothermal heat fluxes[36] applied at the seafloor. The chosen, adjoint-based estimation methodology does not rely on assimilation increments[24] but rather optimizes surface forcing fields and internal model parameters[30,37,38]. As a result, the gridded data product offers closed heat budgets where the convergence of transports matches the ocean state evolution to machine precision[30].

The underlying configuration of the Massachusetts Institute of Technology general circulation model[30,35] uses the 'real freshwater flux' formulation, accounting for mass fluxes across the sea surface associated with precipitation, evaporation, runoff and sea-ice freezing and melting. However, as commonly done in climate modelling, the model makes the Boussinesq approximation and neglects specific heat capacity variations[30,37]. In practice, this means that for any given volume element V, the corresponding heat content is simply given by $H = \rho_c C_p \theta V$ where ρ_c is the constant Boussinesq density, C_p is the constant specific heat capacity and θ is the potential temperature averaged over V. Accordingly, if $\mathbf{U}$ denotes a volume flux across the sea surface or in the ocean interior, then the corresponding mass flux is given by $\mathbf{M} = \rho_c \mathbf{U}$. In this paper, we follow common oceanographic usage by referring to $\rho_c C_p \theta \mathbf{U}$ simply as heat transport rather than as an approximation of total energy transport, which would be more rigorous[25,26].

To derive OHT_0, OHT_∇ and $OHT_{R,0}$, which correspond to $\mathbf{F}$, $\mathbf{F}_{\mathrm{div}}$ and $\mathbf{F}_{\mathrm{rot}}$ in equations (1) and (2), we first sum up all advective and diffusive transports of potential temperature, multiply them by $\rho_c C_p$, and integrate vertically. The 20-year mean transports reported in Figs. 1 and 2 and Supplementary Tables 1–4 are computed by integrating the transverse component of either OHT_0 or OHT_∇ along grid line paths shown in Supplementary Fig. 2. The corresponding 20-year mean $\mathcal{P}$ and $\mathcal{S}$ are depicted in Fig. 3 as, respectively, coloured and grey contours. When computing pole-to-pole meridional transports for the Atlantic, Pacific and Indian oceans (for example, in Fig. 2), the Arctic is split into two sectors along the 80° W and 100° E meridians, the Southern Ocean is split into three sectors along Drake Passage, 147° E and 20° W, and marginal seas are attached to neighbouring oceans as reflected by the colour coding in Supplementary Fig. 2. All required functionalities are provided by the gcmfaces toolbox[30,31].

ERL. Choices of ERL can be a major concern, notably for ship-based OHT estimates, as a result of non-zero mass fluxes[5,13]. Outside this section, we follow the common practice of choosing an ERL at 0 °C (that is, $\theta_{\mathrm{ERL}} = 0$ °C) as reflected by the '0' subscript in OHT_0. To evaluate the impact of such a choice, we recompute equations (1)–(5) but after subtracting $C_p \theta_{\mathrm{ERL}} \mathbf{M}$ from OHT_0, where $\theta_{\mathrm{ERL}} = 3.5$ °C or 18.5 °C and $\mathbf{M}$ is the mass transport from ECCO that includes both rotational and divergent components[33]. This effectively shifts the ERL to 3.5 °C or 18.5 °C—two reasonable choices that correspond to the global mean ocean temperature and sea surface temperature, respectively. The results are presented in Supplementary Fig. 6 and Supplementary Tables 5 and 6.

Differences between the 3.5 °C and 18.5 °C cases are large for plain OHT whereas effective OHT is much less sensitive to the ERL choice (for example, compare Supplementary Tables 5 and 6). This sensitivity contrast reflects that the magnitude of rotational mass fluxes associated with gyres, the Antarctic Circumpolar Current and so on vastly exceeds the magnitude of divergent mass fluxes associated with evaporation and precipitation[30,32]. Accordingly, the streamfunction associated with the rotational component differs wildly between the two panels of Supplementary Fig. 6 and Fig. 3, whereas the scalar potential is remarkably insensitive to ERL choices.

Our results show that both the sign and the magnitude of plain OHT generally reflect arbitrary ERL choices. Heterogeneous treatment of non-zero mass fluxes can, therefore, greatly complicate the interpretation of plain OHT as observed through sections. In contrast, effective OHT changes by less than 0.01–0.02 PW when ERL is changed, and variations of this magnitude are well below other sources of uncertainties (for example, those reported in Supplementary Table 9).

Heat budget. To evaluate uncertainties associated with our interpretation of OHT_∇, it is useful to consider the various terms of the temperature equation computed at constant volume[34]. The underlying heat budget can be written for a time-variable volume element, V, as

$$\frac{dH}{dt} = \rho_c C_p \left(\theta \frac{dV}{dt} + \frac{d\theta}{dt} V \right) \tag{6}$$

where $\rho_c \frac{dV}{dt}$ is the rate of mass flux convergence and $\frac{d\theta}{dt}$ is the rate of temperature change within the selected volume element. More detailed equations are provided elsewhere[30].

The temperature equation computed at constant volume, which is free of any mass flux convergence by definition, expresses the second term on the right-hand side of equation (6) as

$$\rho_c C_p V \frac{d\theta}{dt} = h_{\mathrm{tend}} = h_{\mathrm{adv}} + h_{\mathrm{dif}} + h_{\mathrm{forc}} \tag{7}$$

where h_{adv} represents the advective heat flux convergence, h_{dif} is the diffusive heat flux convergence, h_{forc} is the external forcing due to air–sea and geothermal heat flux convergence, and h_{tend} is the heat content tendency. Any term in equation (7), once its global mean has been removed, can be substituted with $\nabla \cdot \mathbf{F}$ on the right-hand side of the Poisson equation (5) to translate it into a divergent vector field associated with a scalar potential as in equation (3).

A close approximation to OHT_∇ is obtained by applying this approach to $h_{\mathrm{adv}} + h_{\mathrm{dif}}$ (for example, compare Supplementary Fig. 3 with Fig. 2) since the

impact of non-zero mass fluxes on OHT_∇ is generally small (see the ERL section). The residual difference between Supplementary Fig. 3 and Fig. 2 shows little interannual variability and time-mean values of the order of ± 0.1 PW in terms of meridional transports (Supplementary Fig. 4; left) with patterns that resemble those seen in net mass transports[32].

Further unpacking the terms in equation (7) reveals that OHT_∇ primarily reflects a balance between advection and air–sea fluxes (top panels in Supplementary Fig. 5). Isopycnal (that is, lateral) diffusion contributes ± 0.2 PW in the time mean with negligible interannual variability (bottom left) while temporal variations in ocean temperature translate into negligible OHT_∇ for the 20-year average along with ± 0.2 PW interannual variability in the tropics (bottom right). As a result, indirect estimates of annual-mean meridional heat transports based on air–sea flux maps (see Estimate Uncertainty) can approximate OHT_∇ only at best within ± 0.3 PW (Supplementary Fig. 4, right). Such uncertainty levels are comparable to the magnitude of, for example, effective inter-ocean OHTs in Supplementary Table 1.

Estimate uncertainty. Collections of gridded global air–sea heat flux estimates can be used to gauge uncertainties that may affect OHT_∇ estimates. As a first-order approximation, the divergence of OHT balances out regional air–sea heat fluxes (see Heat budget). Effective OHT estimates can therefore be inferred from air–sea flux products by using the Poisson equation approach by replacing $\nabla \cdot \mathbf{F}$ in equation (5) with the air–sea flux estimates. Here we use seven different products in addition to the ECCO estimate of air–sea fluxes (Supplementary Table 7).

The products were obtained from the European Centre For Medium-Range Weather Forecasts (http://apps.ecmwf.int/datasets/), University of Reading (http://www.personal.reading.ac.uk/~sgs01cll/flux/) and the National Center for Atmospheric Research (NCAR; http://www.cgd.ucar.edu/cas/catalog/). The first four NCAR-based products are energy budgets derived from atmospheric reanalysis products (see http://www.cgd.ucar.edu/cas/catalog/newbudgets/ for details) that we converted into air–sea heat flux estimates by adding the net flux at the top of the atmosphere from Clouds and the Earth's Radiant Energy System (CERES; https://ceres.larc.nasa.gov/products.php?product=EBAF-TOA). The resulting estimates start in 2001 as this is the first full year covered by CERES. The University of Reading surface flux product also combines CERES with a reanalysis energy budget. It covers 1985 to 2017 but we focus on 1992 to 2011 as done with ECCO and ERA-interim fluxes. The CORE2-flux estimate is a blended and adjusted product that is based on NCEP reanalysis data[39] distributed by NCAR (https://rda.ucar.edu/datasets/ds260.2/#!access).

Translating each air–sea flux product into an effective OHT estimate via the Poisson equation solver yields Supplementary Fig. 7 and Supplementary Table 9. It is remarkable how much the resulting OHT patterns and values are generally consistent across the set of estimates not only for the global ocean but also for individual oceans—without having to do any adjustment to the air–sea flux products. These diagnostics, in fact, appear quite robust compared to results from earlier OHT inference methods. For example, integrating air–sea heat fluxes southward from the North Pole as explained in the Improved method section can lead to a large spread among estimates (Supplementary Fig. 8). This well-documented issue of integration-based methods[4,5] is readily alleviated by the Poisson-based method (Supplementary Fig. 7).

In turn, one may interpret differences among the Supplementary Fig. 7 estimates as a result of air–sea heat flux uncertainties. The standard deviations reported in Supplementary Table 9 should be regarded with caution because the air–sea flux estimates are not independent from one another—four of them are based on ERA-Interim, five use CERES and all reanalyses share input data sets anyway. Nevertheless, they reflect the order of magnitude of OHT uncertainties induced by air–sea heat flux uncertainties. It is encouraging that values from Supplementary Tables 1–4 are generally close to ensemble means reported in Supplementary Table 9. A noteworthy exception is found between 10° S and 30° N in the Atlantic where the ECCO estimate is smaller, by as much as 0.13 PW, than all other estimates.

On the basis of the Poisson equation output, we can also estimate the convergence and divergence of OHT in any region (for example, Supplementary Table 8) to confirm that divergence from the tropical Pacific is much larger than convergence in the Atlantic and pan-Arctic. Pacific divergence is here computed from maxima in poleward OHT found at ~10° latitude in both hemispheres plus the ITF value. The other term is the convergence between Bering Strait, Drake Passage and the Australia–Antarctica Passage. For the inferred estimates in Supplementary Table 7, the ratio of Pacific divergence to Atlantic plus pan-Arctic convergence is 4.31, 8.26, 3.55, 3.65, 4.14, 3.77, 3.60 and 3.65. For the gridded OHT estimate discussed in the paper, this ratio is $1.8/0.4 = 4.5$.

Improved method. Earlier studies have inferred meridional OHTs by cumulatively integrating air–sea fluxes from the North Pole to the South Pole over the Atlantic, Pacific and Indian. This approach goes back as far as the 1950s[40]. Here we reproduce one such method[7] that prescribes that there is zero OHT through the Indonesian archipelago and the Southern Ocean passages between the Atlantic, Pacific and Indian. The whole Arctic is attached to the Atlantic in this computation, which de facto also sets OHT through Bering Strait to zero.

The result of this computation for ECCO, denoted below as OHT_f, is depicted in Supplementary Fig. 9 (dashed curves). It is in good agreement with Fig. 3 in the earlier study[7] that applied this integration method to a combination of top-of-atmosphere radiation, atmospheric and oceanic products. However, comparing OHT_f and OHT_∇ estimates in Supplementary Fig. 9, which are based on the exact same OHT convergence field, reveals biases in OHT_f (compare the dashed and solid curves).

Starting from the North Pole, the closing of Bering Strait leads to a northward OHT bias in the Atlantic and a corresponding southward OHT bias in the Pacific. In turn, the ITF closing induces a northward OHT bias in the Indian while adding southward OHT bias south of ~10° S in the Pacific. Additional compounding of OHT biases is seen further south as a result of closing Drake Passage and the Australia–Antarctica section.

Once integration has reached the coast of Antarctica, the end result is an unbalanced OHT of 0.39, -0.62 and 0.22 PW for the Atlantic, Pacific and Indian, respectively. These large imbalances are consistent with those previously reported[7], and result from introducing artificial boundaries of integration between oceanic basins. This clearly argues in favour of a more objective approach[7] such as the one introduced in this paper, which readily reconciles artificial differences among estimates (compare Supplementary Figs. 7 and 8).

Code availability
The code used to generate the results in the paper can be accessed from public repositories and permanent archives[31,35]. Maps shown in this paper and Supplementary Information were created using the M_map toolbox[41], available at www.eoas.ubc.ca/~rich/map.html.

Data availability
The data that support the findings of this study are available from the corresponding author upon request and via the Harvard Dataverse https://doi.org/10.7910/DVN/AVVGYX. They are publicly available and permanently archived[33,34].

References
25. Bryan, K. Measurements of meridional heat transport by ocean currents. *J. Geophys. Res.* **67**, 3403–3414 (1962).
26. Warren, B. A. Approximating the energy transport across oceanic sections. *J. Geophys. Res. C* **104**, 7915–7919 (1999).
27. Vranes, K., Gordon, A. L. & Ffield, A. The heat transport of the Indonesian throughflow and implications for the indian ocean heat budget. *Deep Sea Res. II* **49**, 1391–1410 (2002).
28. Watterson, I. G. Decomposition of global ocean currents using a simple iterative method. *J. Atmos. Ocean. Technol.* **18**, 691–703 (2001).
29. Chen, T.-C. Global water vapor flux and maintenance during FGGE. *Mon. Weather Rev.* **113**, 1801–1819 (1985).
30. Forget, G. et al. ECCO version 4: an integrated framework for non-linear inverse modeling and global ocean state estimation. *Geosci. Model Dev.* **8**, 3071–3104 (2015).
31. Forget, G. gcmfaces: A Matlab Toolbox Designed to Handle Gridded Earth Variables Using Compact and Generic Codes (Massachusetts Institute of Technology, 2017); https://doi.org/10.5281/zenodo.834079
32. Forget, G. et al. ECCO Version 4: Second Release (DSpace@MIT, 2019); http://hdl.handle.net/1721.1/102062
33. Forget, G. ECCO Version 4 Release 2: Monthly 1992–2011 Time Series (Massachusetts Institute of Technology, 2016); https://doi.org/10.7910/DVN/NXYKDW
34. Forget, G. ECCO Version 4 Release 2: Three Daily Tendency Terms for Temperature (Massachusetts Institute of Technology, 2016); https://doi.org/10.7910/DVN/T093T1
35. Forget, G. ECCO Version 4: An Ocean State Estimation Framework Based on the MITgcm and its Adjoint (Massachusetts Institute of Technology, 2018); https://doi.org/10.5281/zenodo.1211363
36. Davies, J. H. Global map of solid Earth surface heat flow. *Geochem. Geophys. Geosyst.* **14**, 4608–4622 (2013).
37. Forget, G. & Ponte, R. The partition of regional sea level variability. *Prog. Oceanogr.* **137**, 173–195 (2015).
38. Forget, G., Ferreira, D. & Liang, X. On the observability of turbulent transport rates by Argo: supporting evidence from an inversion experiment. *Ocean Sci.* **11**, 839–853 (2015).
39. Large, W. & Yeager, S. The global climatology of an interannually varying air–sea flux data set. *Clim. Dyn.* **33**, 341–364 (2009).
40. Sverdrup, H. U. in *Handbuch der Physik* (ed. Bartels, J.) Vol. 48 608–670 (Springer, 1957).
41. Pawlowicz, R. *M_Map: A Mapping Package for MATLAB* Version 1.4j (University of British Columbia, 2018).